Simultaneous measurements of a turbulent round jet using PIV and Holographic-PIV

O. Amili[1]**, D. Edgington-Mitchell**[1]**, D. Honnery**[1]**, and J. Soria**[1,2]

[1]Laboratory for Turbulence Research in Aerospace and Combustion, Department of Mechanical and
Aerospace Engineering, Monash University, VIC 3800, Australia
[2]Department of Aeronautical Engineering, King Abdulaziz University, Jeddah, Kingdom of Saudi Arabia
Email for correspondence: omid.amili@monash.edu.au

Abstract

The study of the dynamics of small scale motions in turbulent jets has been of interest. Their contribution to the production, evolution, and dissipation of the kinetic energy is important to understand turbulence mixing, and the turbulent/non-turbulent interface. Holographic PIV/PTV offers a solution to volumetric measurements of complex three-dimensional velocity fields in turbulent flows. This study is aimed to quantify the accuracy of the digital in-line holography in the 90° scattering recording configuration using a previously characterized turbulent jet flow. The Reynolds number based on the mean velocity and diameter at the nozzle exit is in the range of $3,000-6,000$. Results show that the two measurement techniques produce velocity statistics within the uncertainty limits of each other.

1. Introduction

When a coherent reference wave is present simultaneously with the light diffracted by or scattered from an object, both amplitude and phase of the diffracted/scattered light can be recorded. From such a recorded interference pattern, i.e. a hologram, an image of the original object(s) can ultimately be obtained. This makes it possible to find the distribution of seeding particles in a flow field, their displacements, and also their size/shape if required. In spite of the fact that holography has been investigated over many decades since its introduction by Gabor (1949), there are certain limitations that restrict its wide application in fluid diagnostics. Perhaps the most important issue is the depth of focus problem that causes poor axial resolution (normal to the hologram plane) in almost all holographic configurations.

1.1 Depth of focus problem

The depth of focus in holography is referred to the distance where a reconstructed particle remains in focus. While there is not a universal definition available, it is generally considered as the range in which the intensity of a reconstructed particle is higher than its background. Due to the reasons discussed here, this distance is normally $1\sim2$ order(s) of magnitude larger than the original particle diameter.

In a diffraction-limited system, more than 80% of the light intensity of a point source in the far field is concenrated in the Airy disk (van de Hulst H.C., 1981). According to the Fraunhofer diffraction approximation, the light intensity of the Airy disk of a finite particle stays in a depth of:

$$\delta_z = \frac{\beta\lambda}{\Omega^2} \tag{1}$$

where δ_z is the depth of focus, λ is the light wavelength, and Ω is the half angular aperture. β is a coefficient equal to or greater than unity as addressed by (Meng & Hussain, 1995). The half angular aperture in the forward scattering is:

$$\Omega = \frac{\lambda}{d_p} \tag{2}$$

where d_p is the particle size. Hence, the depth of focus is proportional to d_p^2. This issue is important in digital holography due to the spatial resolution and size of the imaging sensor. Even with a recent CCD/CMOS sensor which have a pixel size of $\sim 5\mu m$, the spatial resolution is approximately 50 times lower than photographic emulsions Schnars & Juptner (2002). Hence, the effective angular aperture of a digitally recorded hologram is much smaller than that of film-based holography:

$$\Omega = \sin^{-1}\frac{\lambda}{4\Delta} \approx \frac{\lambda}{4\Delta} \tag{3}$$

where Δ is the pixel size. Equation (3) is derived based on the superposition of two plane waves intersecting with an angle of 2Ω (with respect to each other) at a recording plane, and the use of the maximum resolvable spatial frequency of a digital sensor. Ω in this equation is resolution-limited due to the fact the finite pixel size limits the recording of the hologram's fringe pattern. On the other hand, the size of the imaging sensor limits the angular aperture as follows:

$$\Omega = \tan^{-1}\frac{N\Delta}{2z} \approx \frac{N\Delta}{2z} \tag{4}$$

where N is the number of pixels along Δ, and z is the distance from the object to the recording medium. In this equation, Ω is size-limited.

1.2 Choice of holographic configuration

Due to the limited angular aperture of digitally recorded holograms, various approaches have been investigated to tackle the depth of focus problem including recording multiple views (Sheng *et al.*, 2003; Soria & Atkinson, 2008; Buchmann *et al.*, 2013), and the application of microscopy to holography (Haddad *et al.*, 1992; Sheng *et al.*, 2006; Soria *et al.*, 2008). However, it is possible to considerably decrease the particle elongation by recording the hologram in a side scattering configuration. The approximation in Equation (2) is valid for small recording angles between the reference and the object beams, i.e. in forward scattering. However, according to Mie's theory, there is not a sharp dominant lobe in the scattered light of a particle in a side scattering viewing angle especially at 90°. As a result, the angular aperture of the distributed intensity is much larger in 90° scattering and consequently the depth of focus is much shorter as shown by (Pu & Meng, 2003).

In-line holography is normally referred to in-line recording using a single beam in the forward scattering configuration. This is mainly used due to the simplicity of the experimental setup. However, separate reference and object beams or side scattering configuration can be employed as used here. The forward scattering recording has the advantage of preserving the shape and size of particles. In contrast, a reconstructed particle in the side scattering as shown by Pu *et al.* (2000), is not completely faithful to the particle's original shape and size, but it has much better axial accuracy. Hence, the choice of the holography setup depends on the application and purpose of the investigation, flow depth, seeding density, optical access, etc. For example, when the illuminated volume is relatively thin, or seeding density is not high, or the preservation of particles' size/shape is important, in-line forward scattering can be appropriate. Upon requiring of the highest depth accuracy (normal to hologram plane), side scattering or off-axis holography is required. The side scattering should not be confused with the off-axis holography where the reference and the object beams are combined at a certain angle rather than zero degree.

Despite the higher axial accuracy obtained in in-line holography using a 90° scattering recording geometry, it is not usually used. This is possibly due to the complexity of the optical setup, and additional data analysis

Table 1: The characteristics of polyamide particles used for seeding.

d_p	$d_{p,10\%}$	$d_{p,90\%}$	ρ_p	n	τ_p	Re_p	Stk
(μm)	(μm)	(μm)	(g/cm^3)	(-)	(ms)	(-)	(-)
56	38	77	1.016	1.52	4.85	37	24

required for the particle extraction. In a side scattering system, a number of parameters are important to take into the account. It includes the object and reference optical path lengths, intensity ratio of the object to the reference beam, light polarization, and the size of the seeding particles. Further details are presented in Section 2.2.

In addition to the complications of a side-scattering holography setup, the location of a reconstructed particle may have a transverse separation (in the hologram plane) with respect to the true coordinates that does not exist in a forward scattering system. The aim of the present study is to accurately quantify the performance of holographic PIV in a side scattering configuration using planar PIV in a one-to-one measurement of a turbulent flow. The focus of the study is on the accuracy of the reconstruction in the $x-y$ (hologram) plane. High-resolution holographic PIV and planar PIV are employed for a simultaneous measurement of the velocity field of an axisymmetric air jet. We have previously shown the capability of the in-line holographic technique (e.g Palero *et al.* (2007); Soria & Atkinson (2008); Amili & Soria (2008)), here, the 90° scattering recording geometry is used.

2. Experimental setup and methodology

2.1 Jet facility

In the present experiment, a converging nozzle with an inner exit diameter of 2 mm is used. Compressed air is provided by a bottled gas regulated at the desired pressure. The flow rate is accurately controlled by a needle valve and is measured by an Alicat Scientific mass flow meter. The flow meter has been calibrated against a pitot static tube. The flow is conditioned in a chamber with a honeycomb and a series of wire mesh screens before the nozzle inlet. The use of this large mixing chamber ensures that the seeded flow uniformly enters the nozzle. The nozzle area ratio, i.e. nozzle inlet to nozzle exit area, is approximately 300.

The flow is seeded with solid particles via an in-house made cyclone particle seeder. The solid particles used in this study are in the form of a polyamide powder (Vestosint 2157) with a volume-weighted mean diameter of d_p=56 μm and a density of ρ_p=1.016 g/cm^3. The choice of this type of seeding is discussed in Section 2.2. The particle size distribution is measured using a Malvern laser diffraction particle size analyzer. 10% and 90% of the particles (based on the volume) have the size of less than 38 μm and 77 μm respectively. The Reynolds number based on the mean particle size and the air velocity at the nozzle exit is $Re_p \approx$37. Hence, a correction factor (Israel & Rosner, 1983) is used to estimate the particle relaxation time (τ_p), and the Stokes number (*Stk*). The particle relaxation time is approximately one order of magnitude larger than the characteristic time scale of the flow, τ_f=D/U. Hence, the particles cannot follow the fast fluid oscillations faithfully. The particle details are found in Table 1. This is not an issue here since the primary aim of the present work is to quantify the accuracy of the side scattering holographic PIV compared to the simultaenous measurement of planar PIV in a controlled environment.

The flow has been previously characterized in a number of operating conditions using different measuring techniques (Khashehchi *et al.*, 2013; Toh *et al.*, 2011). In this experiment, lens-less holography with 90° light scattering is used for the velocity measurement. In addition, a PIV system is set up for the simultaneous 2C-2D velocity measurement using the same imaging resolution and field of view. Measurements were taken at a temperature of approximately 20 ^{o}C. The Reynolds number based on the diameter and the mean velocity at the nozzle exit is in the range of 3,000$-$6,000. The measurements are taken at two stations in the regions of $x = 0 \sim 6.6D$ and $x = 6.6D \sim 13.2D$. In the present work, only the Reynolds number of 3,000 case at the first measurement station is presented. A schematic of the experimental setup is shown in Figure 1.
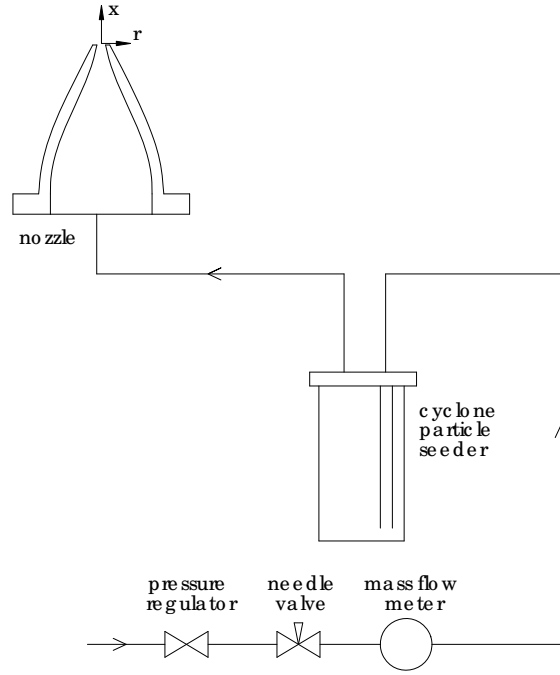
Figure 1: A schematic diagram of the jet rig facility. Note that the dimensions are not to scale.

2.2 *Optical arrangement*

The measurements are performed along the streamwise-radial direction at the center plane of the jet. Two 14-bit CMOS arrays of 2,000 px×2,000 px are used as the imaging sensors. A two-cavity Nd:YAG pulsed laser (532 nm and 420 mJ per pulse) is used as the illumination source. A non-polarizing 95%T-5%R plate beam splitter is used to separate the laser light for the PIV and HPIV optical paths. An appropriate combination of spherical and cylindrical lenses is used to reduce the beam dimater and to produce a collimated light sheet with a thickness of approximately 1 mm. This optical path creates a laser sheet for the PIV camera and also provides the object beam for the Holographic-PIV camera as shown in Figure 2. A 55 mm Micro-Nikkor lens in combination with appropriate extension rings is used to obtain a magnification (M) of unity for the PIV camera. Due to the large size of particles and the high spatial resolution ($\sim 6.5 \mu m$/px), the particle's geometric size mainly dominates the diffraction limited diameter (~ 2.3 px). The mean particle size is approximately 10 pixels using a F-number of 5.6. The depth of field (Δ_z) based on the diffraction limited image diameter, F-number, and the magnification is estimated as $\sim 320 \mu m$ (Raffel *et al.*, 2007). The second optical path provides an expanded laser light acting as a reference beam. A pinhole is positioned at the focal point of the convering lenses to spatially filter out higher order energy peaks to produce a clean Gaussian beam. A 50%T-50%R non-polarizing cube beam splitter combines the reference light with the scattered light from the particles to form a hologram on the imaging plane. The large size of the BS cube (50 mm), provides a large aperture to combine the light beams with no effect of the diffractions from the cube edges.

It is worth highlighting that the coherence length of pulsed Nd:YAG lasers with no injection seeding is usually in the order of 10 mm. Hence, it is very important to set up the reference and the object optical lines very carefully. Unmatched optical path lengths could cause no interference of the object and the reference beams. In addition, the ratio of the intensity of the reference beam with respect to the object beam intensity is quite important. This intensity ratio is adjusted by the use of appropriate neutral density (ND) filters in combination with plate beam splitters. Light polarization is also crucial in this setup for the interference of the object and the reference beams. The light scattered from a linearly polarized incident wave is linearly polarized in the same direction. Hence, both optical paths shown in Figure 2 are set up in the way that the requirement for the same polarization condition is fulfilled.
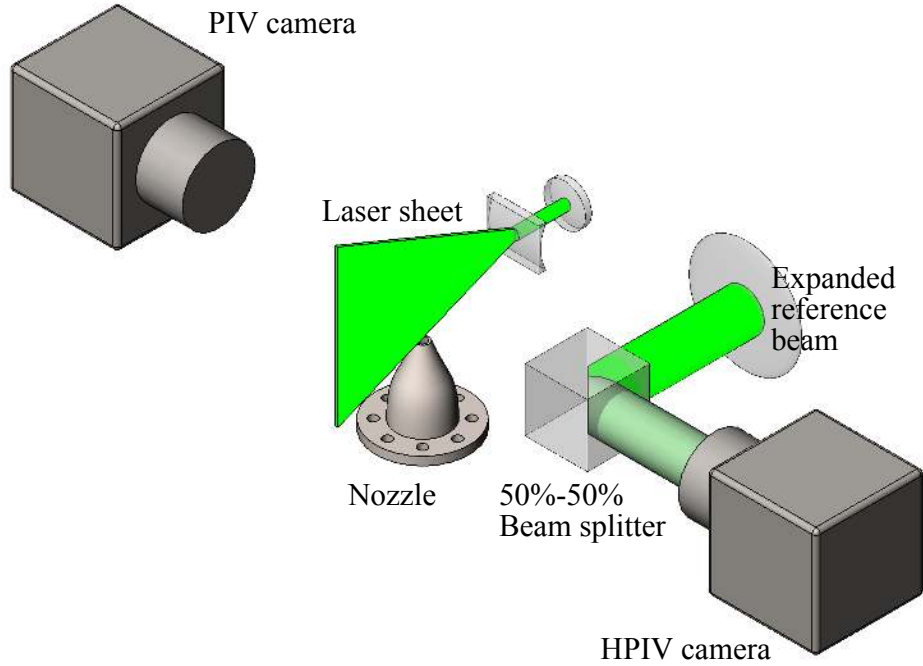
Figure 2: A schematic diagram of the optical setup. Note that the dimensions are not to scale.

As described in Section 2.1, large solid particles are used for seeding the air flow. The scattering efficiency is the highest in a forward scattering view. However, to overcome the depth of focus problem discussed in Section 1.1, 90° side scattering is used in this study. According to Mie's scattering theory (van de Hulst H.C., 1981), the intensity of the scattered light is proportional to the square of the particle diameter. As a result, the use of much larger particles in comparison with oil/water droplets that are normally used in gas flows, significantly enhances the intensity of the scattered light. Hence, this makes the fringe patterns appear larger and clearer in the hologram plane. It also has the advantage that for a given incoming light intensity, more energy is scattered due to a higher value of the refractive index of particles. The distance between the illumination plane and the recording plane is also an important parameter. Since the scattered light from particles travel in a form of diverging spherical waves, i.e. e^{ikz}/z, the light intensity decreases at the rate of $1/z^2$. Hence, to capture more light and to enhance the SNR in a side scattering holographic configuration, it is important that the recording plane is positioned as close as possible to the illuminated volume. In this experiment, due to the geometric constraints, a distance of $z_o \approx 140$ mm between the center plane of nozzle and the CMOS array is used.

2.3 Calibration

In order to calibrate the imaging systems, a calibration grid (1mm×1mm spacing) is accurately located at the center of the nozzle using two micrometer stages. One edge of the PIV image is oriented along the nozzle radial direction and its magnification is set to unity. In the holography view, the illumination beam is parallel to the imaging plane, and consequently mainly light reflection from the glass edges of the grid is recorded, and hence the calibration grid cannot be reconstructed. As a result, an alternative optical path is used to record a hologram of the grid in an in-line forward scattering configuration. The exact magnification of the holographic system is calculated as the ratio of the distance between two intersecting reconstructed grid lines and its true spacing. This way, a slight deviation from a collimated beam can be corrected. In addition, in order to accurately position the HPIV camera chip with respect to the nozzle, an image of a rod as a pointer is recorded. The rod has a sharp tip and is tight fit into the nozzle during the calibration. The field of view for both cameras is approximately 6.6×6.6 nozzle diameter along the streamwise and radial directions.

3. Analysis

3.1 Hologram reconstruction

The object field is numerically reconstructed based on the scalar diffraction theory. The hologram intensity, $H(\xi, \eta)$ is multiplied by a reference wave, $R(\xi, \eta)$ (or its conjugate) and then the resulting wave, $H(\xi, \eta)R(\xi, \eta)$, is numerically propagated to the image plane. Applying Rayleigh-Sommerfeld diffraction theory (Goodman, 2005), the optical field at the image plane $U(x, y, z)$ can be calculated as:

$$U(x,y,z) = \frac{1}{j\lambda} \int \int H(\xi,\eta)R(\xi,\eta)\frac{e^{jkr_{01}}}{r_{01}}\psi d\xi d\eta \tag{5}$$

where k is the wave number ($2\pi/\lambda$), r_{01} is the distance from a point (x, y, z) in the image plane to the point (ξ, η) in the hologram plane, and ψ is an obliquity factor based on Huygens's Principle. It is the cosine function of the angle between the normal line to the reference wavefront and the normal line to the object wavefront. Since the angular aperture of the hologram is small, ψ can be set to unity over the entire hologram.

An equivalent formulation based on the convolution theorem is useful. Equation (5) can be assumed as a convolution between $H(\xi, \eta)R(\xi, \eta)$ with an impulse function, $g(x, y)$, at the plane of z:

$$g(x,y) = \frac{1}{j\lambda}\frac{e^{jk\sqrt{x^2+y^2+z^2}}}{\sqrt{x^2+y^2+z^2}} \tag{6}$$

The application of the convolution theorem states that the Fourier transform of the convolution of HR with g is the product of the individual transforms. The analytical calculation of Fourier transform of function g is (Goodman, 2005):

$$G(f_x, f_y) = e^{jkz\sqrt{1-(\lambda f_x)^2-(\lambda f_y)^2}} \tag{7}$$

As a consequence, $U(x, y, z)$ can be calculated by the Fourier transform of HR, multiplied by G, and finally taking an inverse Fourier transform of the product. The whole process requires two transforms which are carried out using the FFT algorithm per scanning plane (per z value) as:

$$U(x,y) = \mathfrak{T}^{-1}\{\mathfrak{T}\{HR\}G\} \tag{8}$$

The transfer function for a hologram recorded in an in-line side scattering configuration is exactly the same as in an in-line forward scattering holographic system. Hence, the numerical reconstruction process is the same in both configurations.

The signal to noise ratio (SNR) is calculated based on the definition suggested by Goodman (1967):

$$\text{SNR} = \frac{I_0/<I_N>}{\sqrt{1+2I_0/<I_N>}} \tag{9}$$

where I_0 is the reconstructed particle intensity, and $<I_N>$ is the spatial mean of the speckle noise intensity. Equation (9) accounts for the interference of the noise with the reference beam. As described by Pu & Meng (2004), the ratio of the image intensity to the mean noise intensity can be estimated as:

$$\frac{I_0}{<I_N>} = \frac{\pi \tan^2(\Omega)}{\lambda^2 n_s L} \tag{10}$$

where n_s is the seeding density (number of particles per unit of volume), and L the integration length (laser sheet thickness in the present case). $n_s \approx 25$ particle/mm^3 is estimated by the number of particles divided by the reconstructed volume (see Section 3.2). Equation (4) gives the half angular aperture of $\Omega \approx 2.73^o$. Hence, using Equation (9), the SNR is approximately 22 that is larger than the minimum value of 5 suggested by Meng *et al.* (1993).

3.2 Particle 3D locating

The morphology of a reconstructed particle in a side scattering configuration is quite different to a forward scattering system. In forward scattering, a reconstructed particle is considerably elongated forming a relatively axisymmetric cylinder, or a cigar-shape object along the optical axis as has been repeatedly reported in the literature (e.g. Arroyo *et al.* (2001); Meng *et al.* (2004)). In the side scattering, however, as shown by Pu & Meng (2003) astigmatism aberration is associated with this elongation. The elongation is shorter, but the morphology is more complex and is a strong function of the particle's size and shape. Despite the complicated 3D geometry of a reconstructed particle, as shown by Pu *et al.* (2000); Pu & Meng (2003), the error in the particle's centroid calculation is expected to be minimum at 90° in the range of $0-180^o$. Although the highest axial accuracy can be achieved at this scattering angle, it has not been used often as discussed in Section 1.2.

The flowchart shown in Figure 3 describes the process to obtain the 3D distribution of the particle field and their displacements for the current experimental setup. Hologram pairs are recorded as discussed in Section 2.2. A mean image of the reference beam recorded over a number of laser pulses is subtracted from the holograms in order to remove the speckle fringes due to any imperfection existing in the optical path. Then, as described in Section 3.1, the particle field reconstruction is performed in the range of $z = z_o \pm \Delta_z/2$ at 50 planes with a fixed spacing. This is followed by thresholding the reconstructed intensity at a certain level. There is a slight change of the light intensity from pulse to pulse, and the final outcome is sensitive to the chosen threshold level. Hence, it is important to use a normalized threshold level based on the histogram of the intensity for each hologram.

Locating particles' centroid based on the maximum intensity may lead to incorrect locations. This can happen due to the residual intensities of speckles which may have relatively high intensities at certain distinct pixels. Here, the particle's centroid coordinate calculation is based on the assumption that the scattered intensity is higher in positions closer to the center of the particle. Hence, x_{c_i}, the coordinate of the centroid of a particle is calculated by the intensity weighted mean of the reconstructed region as follows:

$$x_{c_i} = \sum_{m=1}^{n_i} x_i I(x_i) / \sum_{m=1}^{n_i} I(x_i) \tag{11}$$

where x_i is the coordinate of a point inside a surrounding volume (V_i), and $I(x_i)$ is the corresponding intensity at that point. n_i is the number of pixels along i direction. The V_i is the volume enclosing a particle based on the edge detection of the reconstructed intensity field at $z = z_o$. It has the size of 24 px$\times$24 px with a depth equal to the number of reconstructed planes (i.e. 50). This step as shown in Figure 3 is taken before the centroid extraction.

The velocity field is then computed using the multi-grid cross-correlation digital particle image velocimetry (MCCDPIV) algorithm developed by Soria (1996). Multi-passing with the final interrogation window size of 96 px$\times$96 px with 50% overlap is used. Due to the large size of particles (i.e. $\sim$ 10px) and the limited number of seeding particles, such a large interrogation region is used. Since the main purpose of this study is the evaluation of the performance of the holographic system in the $x-y$ plane, 2C-2D is used for the simplicity. A 3C-3D cross correlation, however, as described in Atkinson & Soria (2009) can also be used.
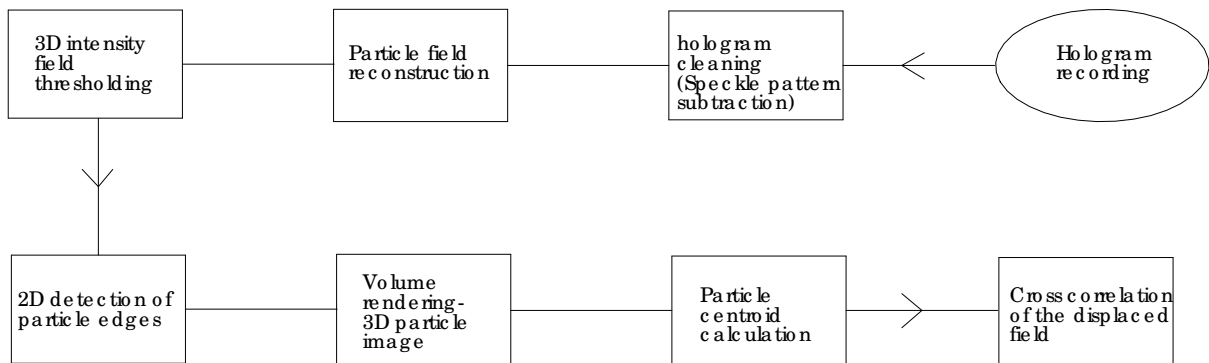
Figure 3: A block digram of the measurement and analysis procedure in the side scattering holography system used here.

4. Results

A typical reconstructed intensity for a sub-field is shown in Figure 4. The iso-surface represents the reconstructed intensity at 75% of the maximum intensity of the hologram. The particle is elongated normal to the hologram plane, but it has a irregular shape with a waist close to its true location. The irregular shape of the reconstructed particle is due to the intrinsic aberration at this scattering angle and cannot be improved by any modification to the optics and their alignment. This complex geometry, which is a function of the particle's size and shape, can be explained by Mie's scattering theory and solving Maxwell's equations using proper boundary conditions as was partially addressed in Pu *et al.* (2000).
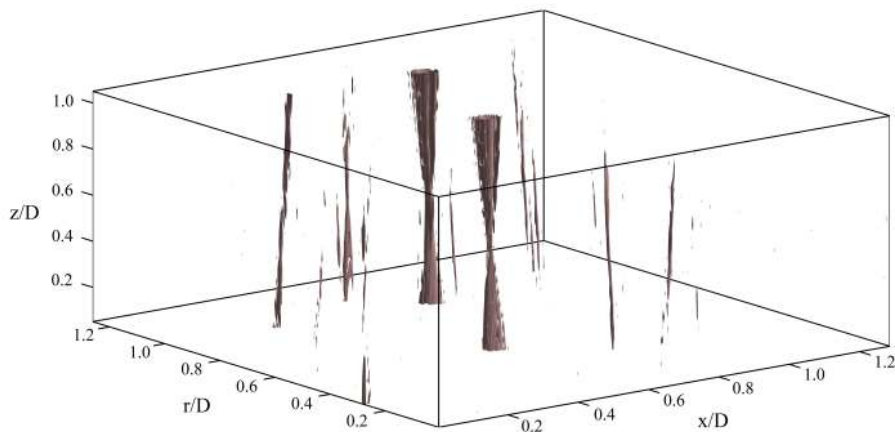

Figure 4: The iso-surfaces of some reconstructed particles.

Before locating the particles' centroid, in order to compare the response of the imaging systems, the point spread function is calculated by the auto-correlation of the particle images. For the HPIV case, to be comparable with the PIV system, the intensity distribution is integrated over the number of z planes reconstructed in the depth of field of the PIV (i.e. in Δ_z). Figure 5 shows the spread function obtained from both measurements compared with a normalized Gaussian intensity distribution. See Raffel *et al.* (2007) for the Gaussian approximation of the particle diffraction. The width of the spread function in the PIV system is approximately 10 pixels

8

which is close the geometric size of the particle (Md_p) that dominates the diffraction limited diameter. In the holographic system, the intensity distribution has a sharper and narrower peak at the center of the reconstructed particle. However, it is wider on sides especially at low intensities. This is possibly due to fringes of the virtual image that still exist in the focused real image.
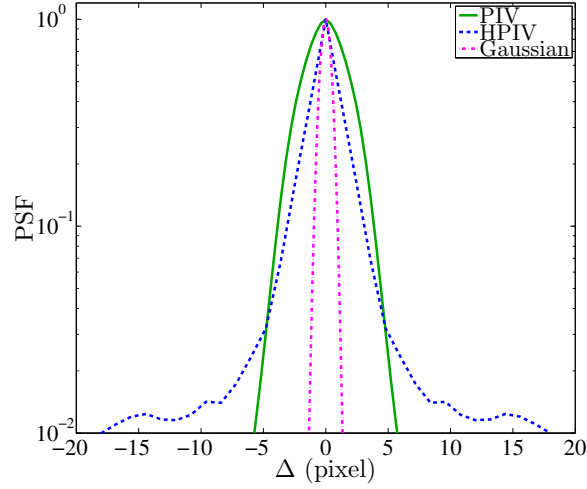

Figure 5: Particle intensity distribution measured by PIV, and HPIV imaging systems. A normalized Gaussian function is shown as an approximation of the diffraction limited imaging. The same magnification and F-number as used in the PIV system is employed to calculate the Gaussian distribution.

An instantaneous velocity field simultaneously resolved by PIV and HPIV is given in Figure 6. The probability density function of the differences between the velocity components measured by two techniques is shown in Figure 7. PDFs are normalized in a way that the integrated area is unity. Figure 7 shows agreement between the measurements since the most probable differences in velocity lie within the range of $\lesssim 0.3$ px and $\lesssim 0.15$ px along the streamwise and radial directions respectively.
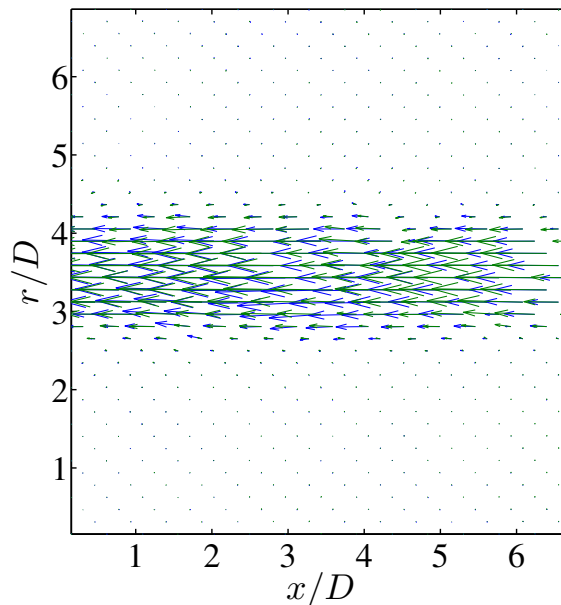

Figure 6: An instantaneous velocity field simultaneously measured by PIV (in green) and HPIV (in blue).

The mean streamwise velocity, and the $< uu >$ fluctuations at a distance of $x/D = 2$ are shown in Figure 8. The largest differences still fall within the uncertainty overlap of the two measurements, and hence there is
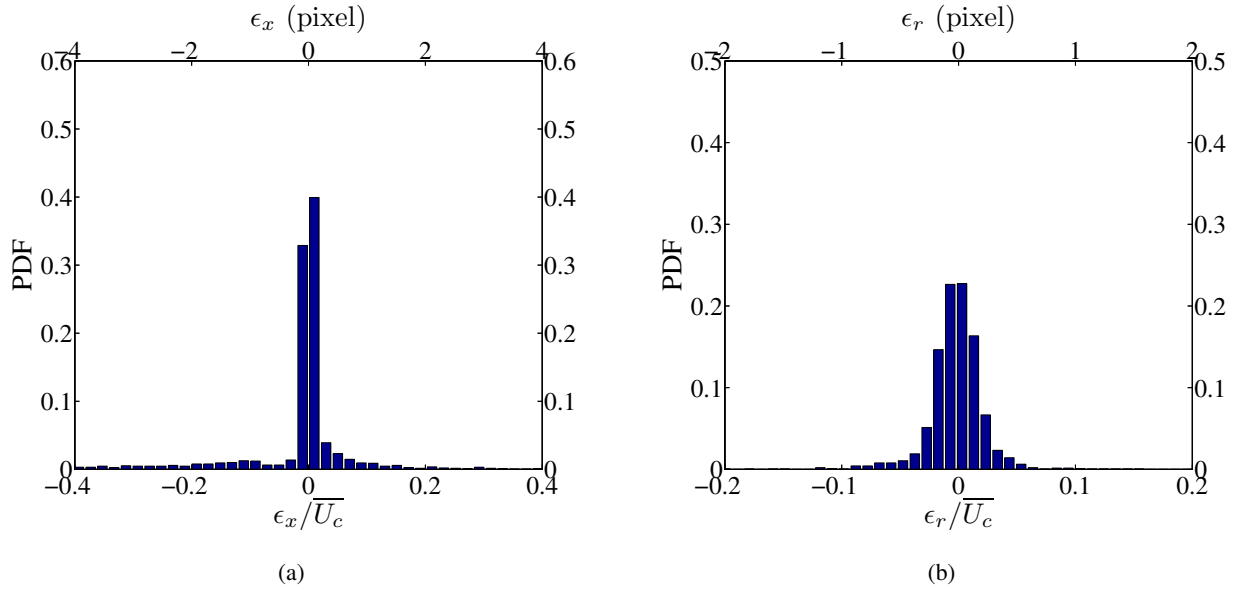
9

Figure 7: PDFs of the difference between the velocity components measured by PIV and HPIV. (a) streamwise velocity (b) radial velocity. ε_x and ε_r represent the difference between the two measurements at the same points along the streamwise and radial directions respectively. $\overline{U_c}$ is the mean axial velocity at the jet exit.

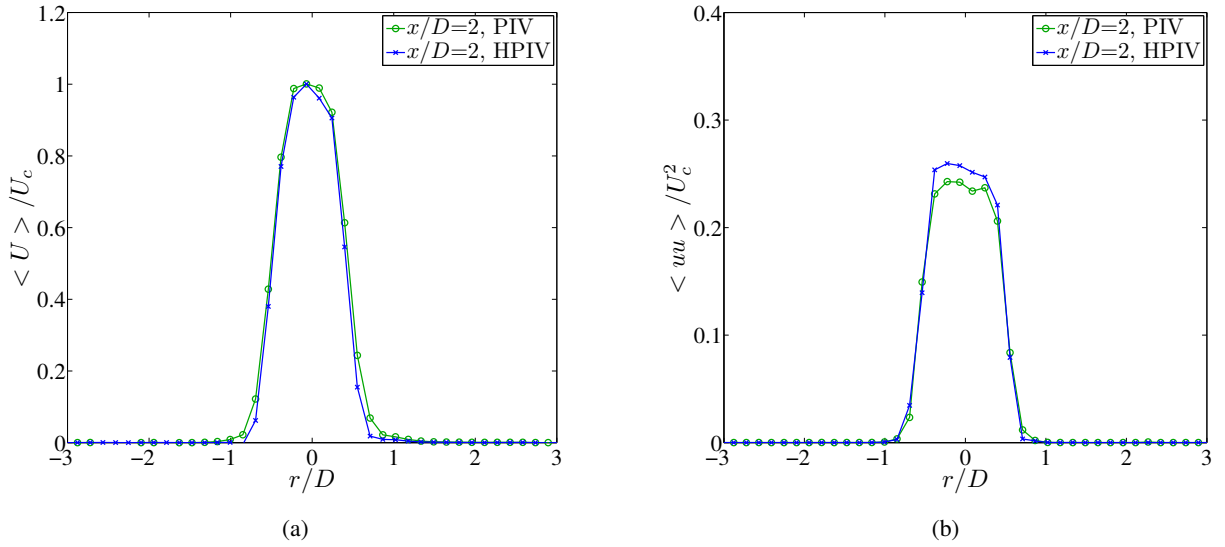statistically no difference in the results from both techniques.

Figure 8: (a) Mean streamwise velocity profile, (b) $< uu >$ Reynolds stress.

5. Concluding remarks

In the present work, a simultaneous measurement of the velocity field using planar PIV and Holographic PIV in the potential core of a turbulent round jet is reported. The study is stimulated by the fact that in side scattering holography, the axial resolution (normal to the hologram plane) is improved in comparison with a forward scattering system, however, the cross section of the particle is not well preserved and hence the lateral resolution is degraded. The evaluation performed here shows that the magnitude of the difference between the velocity components measured by the PIV and holographic systems is ∼0.5 pixel in average (approximately

10

5% of the mean axial velocity).

Acknowledgments

REFERENCES

AMILI, O. & SORIA, J. 2008 Application of digital holographic microscopic piv to a water jet. *Proceedings of the 5ᵗʰ Australian conference on laser diagnostics in fluid mechanics and combustion, Perth, Australia, 3-4 Dec 2008* pp. 51–54.

ARROYO, M. P., VON ELLENRIEDER, K., LOBERA, J. & SORIA, J. 2001 Measuring 3-c velocity fields in a 3-d flow domain with holographic piv and holographic interferometry. *DLR-Mitteilung* (3), 653–658.

ATKINSON, C. & SORIA, J. 2009 An efficient simultaneous reconstruction technique for tomographic particle image velocimetry. *Exp Fluids* **47** (4-5), 553–568, cited By (since 1996): 8.

BUCHMANN, N.A., ATKINSON, C. & SORIA, J. 2013 Ultra-high-speed tomographic digital holographic velocimetry in supersonic particle-laden jet flows. *Meas Sci Tech* **24** (2).

GABOR, D. 1949 Microscopy by reconstructed wave-fronts. *P Roy Soc A-Math Phy* **197** (1051), 454–487.

GOODMAN, J.W. 1967 Film-grain noise in wavefront-reconstruction imaging. *J Opt Soc Am* **57** (4), 493–502.

GOODMAN, J. W. 2005 *Introduction to Fourier optics*, 3ʳᵈ ed. edn. Roberts and Company Publishers.

HADDAD, W. S., CULLEN, D., SOLEM, J. C., LONGWORTH, J. W., MCPHERSON, A., BOYER, K. & RHODES, C. K. 1992 Fourier-transform holographic microscope. *Appl Optics* **31** (24), 4973–4978.

VAN DE HULST H.C. 1981 *Light scattering by small particles*. Dover Publications, New York.

ISRAEL, R. & ROSNER, D.E. 1983 Use of a generalized stokes number to determine the aerodynamic capture efficiency of non-stokesian particles from a compressible gas flow. *Aerosol Sci Tech* **2** (C), 45–51.

KHASHEHCHI, M., OOI, A., SORIA, J. & MARUSIC, I. 2013 Evolution of the turbulent/non-turbulent interface of an axisymmetric turbulent jet. *Exp Fluids* **54** (1).

MENG, HUI, ANDERSON, W.L., HUSSAIN, FAZLE & LIU, DAVID D. 1993 Intrinsic speckle noise in in-line particle holography. *J Opt Soc Am* **10** (9), 2046–2058.

MENG, H. & HUSSAIN, F. 1995 Instantaneous flow field in an unstable vortex ring measured by holographic particle velocimetry. *Phys Fluids* **7** (1), 9–11.

MENG, H., PAN, G., PU, Y. & WOODWARD, S. H. 2004 Holographic particle image velocimetry: From film to digital recording. *Meas Sci Tech* **15** (4), 673–685.

PALERO, V., ARROYO, M. P. & SORIA, J. 2007 Digital holography for micro-droplet diagnostics. *Exp Fluids* **43** (2-3), 185–195.

PU, Y. & MENG, H. 2003 Intrinsic aberrations due to mie scattering in particle holography. *J Opt Soc Am* **20** (10), 1920–1932.

PU, Y. & MENG, H. 2004 Intrinsic speckle noise in off-axis particle holography. *J Opt Soc Am* **21** (7), 1221–1230.

Pu, Y., Song, X. & Meng, H. 2000 Off-axis holographic particle image velocimetry for diagnosing particulate flows. *Exp Fluids* **29** (SUPPL. 1), S117–S128.

Raffel, M., Willert, C.E., Wereley, S.T. & Kompenhans, J. 2007 *Particle Image Velocimetry, A Practical Guide*, 2nd ed. edn. Springer.

Schnars, U. & Juptner, W. P. O. 2002 Digital recording and numerical reconstruction of holograms. *Meas Sci Tech* **13** (9), R85–R101.

Sheng, J., Malkiel, E. & Katz, J. 2003 Single beam two-views holographic particle image velocimetry. *Appl Optics* **42** (2), 235–250.

Sheng, J., Malkiel, E. & Katz, J. 2006 Digital holographic microscope for measuring three-dimensional particle distributions and motions. *Appl Optics* **45** (16), 3893–3901.

Soria, J. 1996 An investigation of the near wake of a circular cylinder using a video-based digital cross-correlation particle image velocimetry technique. *Exp Therm Fluid Sci* **12** (2), 221–233.

Soria, J., Amili, O. & Atkinson, C. 2008 Measuring dynamic phenomena at the sub-micron scale. *Proceedings of the Int conference on nanoscience and nanotechnology (ICONN 2008), Melbourne, Australia, 25-29 Feb 2008* pp. 129–132.

Soria, J. & Atkinson, C. 2008 Towards 3c-3d digital holographic fluid velocity vector field measurement-tomographic digital holographic piv (tomo-hpiv). *Meas Sci Tech* **19** (7).

Toh, C., Treleaven, N., Amili, O., Buchmann, N. & Soria, J. 2011 Coherent imaging and density measurements in supersonic jet flow. *Proceedings of the 9th Australasian Heat and Mass Transfer Conference (9AHMTC), Melbourne, Australia, 2-4 Nov 2011* .